Nonlocal heat transport and improved target design for x-ray heating studies at x-ray free electron lasers

Oliver Hoidn and Gerald T. Seidler

Phys. Rev. B **97**, 035145 — Published 19 January 2018

DOI: 10.1103/PhysRevB.97.035145

Nonlocal Heat Transport and Improved Target Design for X-ray Heating Studies at X-ray Free Electron Lasers

Oliver Hoidn and Gerald T. Seidler(*)

Physics Department, University of Washington, Seattle WA

The extremely high power densities and short durations of single pulses of x-ray free electron lasers (XFELs) have opened new opportunities in atomic physics, where complex excitation-relaxation chains allow for high ionization states in atomic and molecular systems, and in dense plasma physics, where XFEL heating of solid-density targets can create unique dense states of matter having temperatures on the order of the Fermi energy. We focus here on the latter phenomena, with special emphasis on the problem of optimum target design to achieve high x-ray heating into the warm dense matter (WDM) state. We report fully three-dimensional simulations of the incident x-ray pulse and the resulting multielectron relaxation cascade to model the spatial energy density deposition in multicomponent targets, with particular focus on the effects of nonlocal heat transport due to the motion of high energy photoelectrons and Auger electrons. We find that nanoscale high-Z/low-Z multicomponent targets can give much improved energy density deposition in lower-Z materials, with enhancements reaching a factor of 100. This has three important benefits. First, it greatly enlarges the thermodynamic parameter space in XFEL x-ray heating studies of lower-Z materials. Second, it allows the use of higher probe photon energies, enabling higher-information content x-ray diffraction (XRD) measurements such as in two-color XFEL operations. Third, while this is merely one step toward optimization of x-ray heating target design, the demonstration of the importance of nonlocal heat transport establishes important common ground between XFEL-based x-ray heating studies and more traditional laser plasma methods.

(*) seidler@uw.edu

Submitted 4/13/2017 Physical Review B
Resubmitted 8/29/2017
Resubmitted 12/28/2017

I. Introduction

Dense matter under extreme conditions of pressure (P), temperature (T), or both, is a topic of classic and growing interest across multiple subfields of contemporary science. [1-5] The development of x-ray free electron lasers (XFELs) is playing a growing role in this field, both when coupled with high-powered lasers in pump/probe studies [6,7] and also via direct x-ray excitation into strongly non-equilibrium states. Important, early work on XFEL-generated extreme conditions considered atomic clusters, where charge separation combines with Coulomb confinement to create extreme ionization states. [8,9] Much subsequent work, on the other hand, considered equally intense illumination of solids [10,11] where fast screening and electronic response preclude Coulomb confinement effects and instead results in a more traditional dense-phase energy relaxation cascade, especially when the illumination spot size is large compared to characteristic energy deposition lengths.

We focus here on the very specific case of femtosecond-scale x-ray heating of crystalline matter, in which there is growing evidence that the lattice often has limited opportunity to structurally relax during the incident x-ray pulses [12-14] and that the loss of crystallinity during the x-ray pulse may have only modest scientific impact. [15] Experiments of this type have spanned a wide range of materials and physical conditions; pioneering examples include the first demonstration of saturable absorption in a solid-density, crystalline Al plasma and direct measurement of the ionization potential depression in a variety of metals and their associated oxides. [16,17]

Such studies hold a significant and, we propose, unique position for discovery, because they encompass the case in which the consequences that traditional condensed phase electronic structure theory has on the structure of partially-ionized plasmas will be strongest and most easily interrogated. Hence, the study of crystalline matter at ambient density but highly elevated electronic temperature holds high potential for directly testing foundational issues in finite-T density functional theory, especially including the proper treatment of T-dependent functionals. [18-20]

This point has recently been made by Valenza and Seidler [20], who demonstrated that finite-T DFT makes strong, initially counter-intuitive predictions about the evolution of the absolute and relative Bragg peak intensities in x-ray diffraction (XRD) from crystalline matter as a function of electronic temperature on the 1 – 50 eV scale. The key point is that XRD provides a more detailed interrogation of the population of electronic states for crystalline matter than it does for the more amorphous states interrogated after, e.g., laser shock heating. Furthermore, it is this temperature dependence that is a key *microscopic observable* of all finite-T DFT approaches: the central quantity calculated in DFT is, after all, the spatial distribution of electron density. Therefore, careful characterization of the real-space charge density at elevated electronic temperatures in a cool lattice gives a direct path to evaluating different DFT implementations. This is particularly significant as regards the temperature-dependent exchange functional, which is essential to predictions of bulk thermodynamic and elastic properties [18,19,21].

However, in such a research program there is a confounding detail. The most effective heating by x-rays will occur with lower-energy photons (that are more strongly absorbed) whereas any detailed interrogation of the real-space charge distribution by XRD requires the use of higher energy x-rays to obtain information over a wide momentum transfer range. [20] This dilemma raises a question that is new in the XFEL community but old in the broader plasma physics community: *Given the incident pulse characteristics and the desired sample material, how does one design a target to achieve optimal energy density deposition*?

The most comprehensive treatment of this question would include a fully spatio-temporal treatment of radiative transport as well as electronic dynamics and electron-atom interactions wherein, again because of the short time scales, lattice relaxation can be ignored or at least is secondary. Within this framework, the temporal evolution of electron-electron and electron-atom interaction includes several stages. First, the atomic physics of the core levels gives rise to an initial population of high-energy Auger electrons and photoelectrons that decay into low-energy (< 50 eV) electronic excitations (both collective and single-particle) on the scale of a few fs. The resulting collective excitations decay by generating electron-hole pairs on the time scale of tens of fs.. Subsequent electron-electron thermalization occurs on the scale of 100 fs – 1 ps

for ambient matter [22-25], but in general has a strong eV-scale temperature dependence, thus requiring a self-consistent treatment at high incident flux levels.[23]

Here, we take a simpler approach with the goal of identifying and illustrating the most important contributors to x-ray heating and how their spatial extent strongly influences optimum x-ray heating target design, in the limited sense of optimizing the deposited net energy density in the desired sample phase. Specifically, we address the key questions surrounding nonlocal energy transport by hot electrons. This topic has a long history in plasma physics, especially for inertial confinement fusion target design, but enters here with typically lower-energy electrons, i.e., keV-scale, than are important in ICF and in direct-drive laser-heating studies. This causes the energy deposition length of the hot electrons to decrease from the 100-1000 μm scale for MeV electrons in laser experiments to instead only ~50-200 nm, depending on the atomic number of the species present in the XFEL x-ray heating target.

It is this much shorter length scale that brings us to consider multicomponent nanoscale targets for x-ray heating so that the influence of nonlocal energy transport by the hot electrons can be usefully engineered. While the importance of nanoscale energy transport has not previously been discussed in the context of XFEL heating target design, it has been studied and exploited in other experimental contexts. For example, there exists a significant body of literature in the medical physics community concerned with using gold nanoparticles for dose enhancement in radiotherapy treatment. [26,27] A contrasting application of nonlocal energy transport is found in the macromolecular crystallography community, where there is interest in the use of submicron incident x-ray beams so that a large fraction of high-energy electrons escape the beam spot before slowing down, thus reducing radiation damage in the probed sample volume. [28-32]

With the above context established, we consider here a nanostructured target design that enhances energy deposition in a sample material using nonlocal heat transport from a more strongly x-ray absorbing material in contact with the sample – we refer to this second material as a ‘cladding’ as a matter of convenience, for closer contact to the terminology of laser-shock target design, even when the geometry may not strictly be cladded. Fig. 1 sketches several corresponding geometries, but in the current paper we concentrate on the particularly simple one of Fig. 1 (c), consisting of a single thin film of sample material clad with Au. Similar layered

target configurations have been explored by Ping, *et al.* [33] for different scientific reasons and on much longer time scales in short-pulse laser experiments, where the inhomogeneous heating established the large temperature gradient needed for thermal conductivity measurements on ps time scales in isochorically heated matter at many-eV temperature.

Here, we use the Monte Carlo code PENELOPE [34] to simulate three-dimensional electron-photon transport in layered targets. The resulting spatial distributions of deposited energy demonstrate two benefits to the design: first, it significantly enhances in-sample energy deposition, and second, it relaxes constraints on XFEL pump photon energy in a way that substantially increases the information content of XRD measurements in important experimental contexts.

We proceed as follows. In section II, we describe the methods used to simulate photoionization and electron transport in a nanostructured target and discuss the simplifying approximations on which we rely. In section III, we present and discuss simulation results of multilayer targets consisting of sample material clad on one or two sides with gold. We find that such a cladding configuration significantly increases deposited energy density in a sample material, with the largest enhancement in low-Z samples. We argue that this enhanced effect in low-Z samples opens the door to wide-angle x-ray diffraction (wide-angle XRD), with significant utility for studying the time dynamics of the energy relaxation cascade for both electronic and lattice/ion degrees of freedom in such materials. These observations are particularly relevant in the context of two-color x-ray pump x-ray probe experiments at XFELs[35-39], but also serve more generally to establish the importance of nanoscale nonlocal heat transport in high-intensity XFEL studies. Finally, in section IV we conclude.

II. Methods

The simulation of electron transport in condensed matter is an area of ongoing research. In addition to continuing development of well-established codes in the high-energy experimental particle physics community [34,40], new developments include incorporation of *ab initio* band structure calculations in order to accurately model the electron mean free paths of interband transitions and plasmon excitations from relativistic energies down to a few eV. [41,42]

In the regime relevant to the present study, calculation of the spatial distribution of deposited energy caused by absorption of a hard x ray requires accurate treatment of the processes that describe scattering of photo- and Auger electrons at the 100 eV to 10 keV scale (generation of secondary x-ray photons, though present, plays a negligible role in energy transport). The simplest atomic treatments of elastic and inelastic scattering demonstrate that, for mid- and high-Z elements, the ratio of elastic to inelastic total cross sections is of order unity and that characteristic elastic scattering angles are sufficiently large (for instance, of order 1 rad for ~1 keV electrons) to influence deposited energy distributions. [43] Both components, therefore, must receive accurate treatments to adequately model spatial energy deposition distributions in a nanostructured target.

The spatial distribution of deposited energy is determined by the electron stopping power dE/dz, which in a classical treatment is related to a material's dielectric function $\varepsilon(q,\ \omega)$ by

$$\frac{dE}{dz} = \frac{2\hbar^2}{\pi a_0 m_0 v^2} \iint \frac{q_y \omega\ Im[-1/\varepsilon(q,\omega)]}{{q_y}^2 + (\omega/v)^2} dq_y d\omega, \quad (1)$$

where ω is angular frequency, q is momentum transfer (with q_y the magnitude of the component for momentum transfer perpendicular to the z-direction), a_0 is the Bohr radius, m_0 is the electron mass, and v is the electron velocity. [43] In the case of electron showers generated by 5-10 keV photons, the electron stopping power's dependence on v causes nonlocal energy transport to be dominated by the highest-energy Auger and photoelectrons. Though the slower time evolution of the subsequent electronic and lattice dynamics may be neglected in the present context of simulating fs-scale energy transport, the possibility of interrogating it by time-resolved XFEL pump-probe measurement is an interesting topic in its own right.[35,36]

To model the above physics we used the code PENELOPE, which implements particle-tracking Monte Carlo simulations of electron showers generated by x-ray photoionization.[34] PENELOPE uses total and differential cross sections based on several physical models. Briefly, it derives elastic and inner-shell inelastic cross sections from strictly atomic wave functions, while the valence contribution to the inelastic double differential cross section is based on the Born approximation and generalized oscillator strength model of Liljequist [44,45], with an energy loss-dependent normalization that allows the model to replicate empirical stopping power

data (provided as program input). Although the inelastic scattering cross section is dominated by low-energy loss collisions, inner shells contribute the majority of the stopping power for several-keV electrons, which account for the longest-range energy transport. For electrons of those energies the stopping power of a compound may be approximated within five percent by a stoichiometric sum based on atomic treatments of its constituents (an observation referred to as Bragg's rule). [46] Consequently we employed material data files generated by the PENELOPE 2011 program MATERIAL, which applies this approximation to infer stopping powers of arbitrary compounds using data from the NIST ESTAR database. [34,47] The PENELOPE simulation's output of interest is the spatial density of deposited energy, $\rho\,(\vec{r})$. Given the planar geometry of the simulated targets, we additionally define a characteristic transport length l based on $\rho\,(\vec{r})$, specifically $l = \int_{z=0}^{\infty} \mathrm{z}(\vec{r})\ \rho\,(\vec{r})\ d^3\vec{r}$.

It should lastly be noted that PENELOPE emits photoelectrons isotropically, whereas in reality the distribution of initial primary photoelectron orientations is proportional to $\cos^2\theta$, where θ is the angle between the photoelectron emission direction and incident photon polarization vector. The impact of this anisotropy has been considered by Sanishvili et al. and others [29,32] in the context of assessing radiation damage of protein crystals under illumination by microfocused x-ray beams. Although anisotropy in the initial distribution of photoelectrons is strong, Sanishvili, et al. [32] have observed that the anisotropy of the damage distribution in protein illuminated by a 0.84 micron-FWHM beam with 18.5 keV photon energy is weak. This is furthermore consistent with their Monte Carlo simulation of this experimental configuration, which showed only a 20% difference between the widths of the energy dose distributions about the incident beam axis in directions parallel and perpendicular to the polarization vector. Although the findings of Sanishvili et al. endorse the position that the XFEL polarization's influence on spatial distributions of deposited energy can be neglected, it may be interesting to investigate the consequences of XFEL polarization in layered high-Z/low-Z systems, where the consequences of anisotropic photoelectron emission will be strongest relative to alternative (non-planar) target geometries.

Given that the smearing of the energy transport with respect to the $\cos^2\theta$ direction about the polarization direction will happen fully isotropically in three dimensions, it follows that there is only modest anisotropy in energy transport between the polarization direction and that of the

initial photon propagation. That being said, the present simulations represent the most extreme case, of those in Fig. 1, where omitted polarization effects could play some role. We note that inclining the sample to the beam, as a practical matter, can largely obviate these concerns. In any event, there is considerable evidence that polarization effects on the primary photoelectron will have quite limited impact on the present class of energy transport problem over length scales of tens of nm using much larger incident beams.

III. Results and discussion

We now present results for a few realizations of our nanostructured target design, all of which consist of thin films clad with Au on one or both sides, i.e., Fig. 1(c). The heating of diamond and Fe thin films via nonlocal heat transport by hot electrons is illustrated in Fig. 2, which shows a two-dimensional projection of electron trajectory traces in two trilayer targets, containing clad C and Fe films, stimulated with 7 keV incident photons. Note that, for improved presentation, only 10% of the tracks beginning in the Au are included for Fig. 2(a), i.e., the Au-C-Au trilayer. The principal observation in both targets is that a large concentration of high-energy photo- and Auger electrons is generated in the Au cladding, and that these electrons have transport lengths on the order of tens of nm, resulting in a significant flux of high-energy electrons across the cladding-sample interface. The consequences of this effect are strongest in the diamond target, where the difference between the photoelectric cross sections of the cladding and interior layer is largest. Only two photoionization events occur in the diamond wherein inelastic scattering of hot electrons originating from the cladding overwhelmingly dominates the energy deposition.

This is quantified by Fig. 3, which compares the linear energy deposition of several Au-C-Au trilayer configurations to that in bare C. The units for the linear energy density deposition per unit incident photon energy, and the quantity itself, deserve some brief comment. The characteristic energy deposition lengths (10-100 nm) in any such hard x-ray study are necessarily much smaller than achievable spot sizes for all but the most extreme focusing achievable at present at the Linac Coherent Light Source, i.e., perhaps 0.5 μm at 7 keV. Consequently, there are no 'interesting' transverse effects here as spot size is varied. The choice of linear energy density deposition per unit incident photon energy, while nontraditional, loses no information but provides a basis for calculation of the experimentally-relevant volumetric

energy density for any chosen incident pulse energy and spot size -- one need simply multiply by the incident flux density having its necessary dimensions of energy per unit area.

Returning to Fig. 3, photoionization by 7 keV photons yields characteristic transport lengths l of 15.0 nm and 72.6 nm, respectively, in simulated bare Au and bare diamond targets. Consistent with the former value, we found that absorbed energy density in the diamond inclusion saturates beyond an Au cladding thickness of 50 nm. Fig. 3 (a) shows the deposited energy distribution in a bare diamond target and in several Au- diamond-Au trilayers with varying thicknesses of the diamond inclusion. An interior layer thickness of 50 nm results in a factor of 100 increase in deposited energy density relative to the bare diamond target. This large enhancement derives from the contrast between the photoelectric cross sections of the high-Z cladding and low-Z sample material.

Such enhancements in energy deposition increase the accessible thermodynamic parameter space in all XFEL heating experiments. This is particularly significant for experimental diagnostics that require deviation from optimal pump pulse characteristics and are therefore normally incompatible with heating studies. XRD studies of low-Z materials such as diamond and graphite are a concrete, and germane, example. Prior XFEL heating studies of these materials have required incident photon energies below 3 keV to reach HED conditions (> ~1 eV temperatures) due to weak absoption in the hard x ray (photon energy > 5 keV) regime. This restriction limits the kinematically accessible range of momentum transfers in XRD, which correspondingly reduces available information on real-space charge density.

This creates an experimental dilemma with scientific consequences. For example, Hau-Riege et al.[10] showed evidence for ultrafast melting of graphite during a 40-fs long XFEL pulse but were limited, for the reason described above, to using 2 keV incident photons thus yielding diffraction from only the (002) Bragg reflection of graphite. The authors interpreted quenching upon heating of the (002) peak as evidence of nonthermal lattice melting. However, Valenza *et al.*[20] questioned this conclusion based on simulated diffraction using frozen-core finite-T DFT calculations, which predicted strong quenching of the graphite (002) reflection due to purely electronic reorganization in crystalline graphite at 10 eV electronic temperature. In graphite and other low-Z systems, the only means of unambiguously separating lattice disorder from

electronic heating in the XRD signal is to probe several Bragg peaks, including the lowest-order reflections and their harmonics. [20]

It is therefore interesting to consider the possibility of doing a wide-angle XRD measurement in which the clad target configuration is used to compensate for the loss in deposited energy density that results from the use of a high incident photon energy. Fig. 3 shows that the deposited energy densities in the interior layer of an Au-C-Au target stimulated by 7 keV photons is a factor of more than four greater compared to an unclad sample heated by 2 keV photons. The stronger indirect heating in the former configuration thus more than offsets the reduction in direct absorption at the higher incident photon energy, making wide-angle XRD viable. In the case of carbon, this benefit comes at the cost of unfavorable signal to background due to the weakness of the XRD contribution from C compared to Au. In the special case of graphite, this can be uniquely compensated for with a highly-oriented pyrolytic graphite (HOPG) sample, whose high-reflectivity 00*l* peaks yield much higher signal to background ratios than the powder-like Bragg and thermal diffuse scattering of polycrystalline Au. Similar configurations exploiting mosaic or single-crystal samples may enhance wide-angle XRD on a variety of low-Z systems, offering a much-improved ability to experimentally test predictions of finite-T DFT-based modeling of electronic structure in low-Z condensed matter, where finite-T effects are easiest to identify because of the relatively large valence-electron contribution to the XRD signal.[20]

Next, in Fig. 4, we show the consequences of XFEL heating of an Au-Fe_3O_4-Au configuration, where we choose ferromagnetic Fe_3O_4 as a likely material where an interesting sequence of valence-level reorganizations will happen at eV-scale temperatures, i.e., spin-flip following by d-band delocalization as electronic temperature increase. In Fig. 4 (a) we provide the analogous results to Fig. 3 (a). There is again a significant enhancement with respect to the bulk (unclad) absorption for incident 7 keV photons, just below the Fe K-edge, although this enhancement is naturally much smaller than for a light species such as C. In Fig. 4 (b) we quantify the inhomogeneity of energy deposition in the central layer. Unsurprisingly, given the characteristic transport lengths here, there is some predicted inhomogeneity. However, some degree of local thermalization seems certain to ameliorate issues on the relevant length scale of ~10 nm.

The above discussion establishes that multicomponent nano-scale x-ray heating targets will, in fact, result in new nonlocal heat transfer effects that can be engineered to the benefit of the experimenter. However, there are several subsidiary issues influencing future experiment design that deserve specific consideration.

First, the scientific benefit here requires not just high enhancement in deposited energy density relative to the bare sample illuminated with high-energy photons, but instead *sufficient* enhancement to reach the several-eV temperatures needed to, e.g., see the valence electronic reorganization effects of the type predicted by Valenza et al. [20] Direct calculation of the dependence of temperature on deposited energy density is difficult, as it requires modeling of the equation of state to many-eV temperatures, itself an open research problem. However, a fairly direct connection can be made with temperatures inferred in an earlier experimental studies of x-ray heating of solids. Based on x-ray Thomson scattering results, Hau Riege et al. estimate temperatures between 1 and 10 eV in a graphite target heated by LCLS pulses with 2 keV photon energy. Although our simulations address a different phase of carbon (diamond), absorbed energy *per atom* is independent of density. The difference in the scaling of temperature as a function of deposited energy density in graphite compared to diamond thus depends only on the contrast between the relevant equation of state for the two phases, which is expected to be of order unity. Returning to Fig. 3, the linear energy density deposition in bare diamond is shown for both 2 keV and 7 keV incident photons. There is the expected factor of ~30 decrease with increasing incident photon energy, but the nonlocal heat transport from the Au cladding to the C filler is predicted to more than overcome this effect. Consequently, the 7 keV experiment on the Au-C-Au target should be expected to achieve similar or somewhat higher temperatures than in the 2 keV experiment on bare graphite, if similar incident flux density is used. Hence, the enhanced energy density deposition from hot electron transport in multicomponent, nanoscale targets is indeed nontrivial, and is expected to achieve the necessary temperatures to see interesting effects from valence-charge reorganization in low-Z materials at ‘tepid’ dense matter temperatures.

Second, in the more general case of a low-Z sample, the viability of an XRD measurement is dependent on a sufficiently low-magnitude of diffuse scattering and fluorescence from the cladding, as well as on the absence of overlap between Bragg peaks of the sample species and

cladding. The experimental signal-to-background ratio becomes more favorable with higher-Z (i.e. more strongly scattering) sample species—with the tradeoff, however, of smaller heating enhancements. The comparison of Au-Fe-Au and Au-C-Au in Figs. 3 and 4, respectively, illustrates this. Note that for the case of an Au cladding at the present incident energies the M-shell fluorescence from the cladding will be strongly rejected by the usual aluminized mylar cover on any experiment's position sensitive detector; such contribution is therefore omitted from the results presented.

Third, in x-ray heating experiments of both mid- and low-Z compounds it is useful to maximize energy deposition by selecting incident photon energies modestly above a strong absorption edge of a dominant atomic species in the sample. In the case of mid-Z targets this choice does not directly conflict with performing wide-angle XRD measurements; however, *K*-shell fluorescence can generate substantial backgrounds, reducing the XRD signal's information content. In such cases nonlocal heating in a structured target can obviate the need for pump photons above the K-edge binding energy, improving the XRD diagnostic's quality. Fig. 5 illustrates this by comparing (1) the energy deposition in Au-Fe-Au and Au-Fe_3O_4-Au targets stimulated with photons below the K-edge of Fe to (2) the energy deposition in a bare Fe target heated by photons above the edge. Nonlocal heating of the former samples compensates for the reduction in heating caused by lowering the incident photon energy below the Fe K-edge; the multicomponent targets thus allow improving the ratio of signal to (fluorescence) background while—in the more favorable case of Fe_3O_4–maintaining an energy deposition density comparable to the highest level possible with an equivalent monolithic target. On the other hand, this comes at some price. In Fig. 6 we show the calculated XRD patterns for the different experimental configuration and conditions. The aforementioned disadvantage of the cladding's presence is clear: the diffracted signal from Au is stronger than that from the interior sample material, making the described reduction in background worthwhile only given weak diffuse scattering and fluorescence from the cladding and sufficient separation between Bragg peaks of the sample and cladding.

Finally, the simulations presented in this paper constitute a first demonstration of a particularly simple implementation of structured target design. One can imagine several improved designs that achieve the same level of nonlocal sample heating while averting some of

the disadvantages of our multilayer approach. For example, a uniform mixture of small (< 50 nm diameter) sample and heater nanoparticles would show similar mean deposited energy densities to a multilayer target and can be prepared by, e.g., spin coating or drop-casting. Such targets would have more homogeneous heating and would additionally allow preparation of much thicker targets and give much higher scattered intensities. A similar result may be possible using electrochemical or vapor deposition to embed sample materials inside porous high-Z metal substrates.[48,49] Two-color XFEL experiments may also lend themselves to lithographically patterned designs with concentric cylindrical volumes of (inner) sample and (outer) cladding materials, wherein the more tightly-focused probe pulse would be inscribed in a volume free of cladding material. Such a configuration would have the intention of reducing (cladding) background relative to signal, which would be particularly useful for weakly-diffracting low-Z samples.

IV. Conclusion

We model the spatial distribution of deposited energy in nanostructured targets for hard x-ray XFEL heating experiments using the Monte Carlo code PENELOPE. We find that two-component targets consisting of a sample material and high-Z cladding achieve substantial nonlocal heating of the sample via the relaxation cascade following transport of multi-keV Auger and photoelectrons. We argue that this target design approach will bring substantial benefits to XFEL heating experiments in the following ways: first, by enlarging their accessible thermodynamic parameter space and second, by improving the capability of x-ray diffraction diagnostics to characterize finite-temperature electronic structure and to distinguish between thermalization of the electronic and lattice degrees of freedom in crystalline warm dense matter systems.

Acknowledgements

We thank Joshua Kas for useful discussions. This work was supported by the United States Department of Energy, Basic Energy Sciences, under grant DE-SC00008580 and by the Joint Plasma Physics Program of the National Science Foundation and the Department of Energy under grant DE-SC0016251.

References

[1] R. P. Drake, *High-Energy-Density Physics: Fundamentals, Inertial Fusion, and Experimental Astrophysics* (Springer, 2006), Shock Wave and High Pressure Phenomena.

[2] S. Krishnan, S. Ansell, J. J. Felten, K. J. Volin, and D. L. Price, Physical Review Letters **81**, 586 (1998).

[3] J. J. Fortney, S. H. Glenzer, M. Koenig, B. Militzer, D. Saumon, and D. Valencia, Physics of Plasmas **16**, 041003 (2009).

[4] S. Glenzer and R. Redmer, Review of Modern Physics **81**, 1625 (2009).

[5] R. C. Davidson, Frontiers in High Energy Density Physics: The X-Games of Contemporary Science 2003.

[6] J. M. Glownia, J. Cryan, J. Andreasson, A. Belkacem, N. Berrah, C. Blaga, C. Bostedt, J. Bozek, L. DiMauro, and L. Fang, Optics express **18**, 17620 (2010).

[7] S. Glenzer, L. Fletcher, E. Galtier, B. Nagler, R. Alonso-Mori, B. Barbrel, S. Brown, D. Chapman, Z. Chen, and C. Curry, Journal of Physics B: Atomic, Molecular and Optical Physics **49**, 092001 (2016).

[8] H. Thomas, A. Helal, K. Hoffmann, N. Kandadai, J. Keto, J. Andreasson, B. Iwan, M. Seibert, N. Timneanu, and J. Hajdu, Physical review letters **108**, 133401 (2012).

[9] L. Young, E. Kanter, B. Krässig, Y. Li, A. March, S. Pratt, R. Santra, S. Southworth, N. Rohringer, and L. DiMauro, Nature **466**, 56 (2010).

[10] S. P. Hau-Riege, A. Graf, T. Döppner, R. A. London, J. Krzywinski, C. Fortmann, S. H. Glenzer, M. Frank, K. Sokolowski-Tinten, M. Messerschmidt *et al.*, Physical Review Letters **108**, 217402 (2012).

[11] P. Sperling, E. Gamboa, H. Lee, H. Chung, E. Galtier, Y. Omarbakiyeva, H. Reinholz, G. Röpke, U. Zastrau, and J. Hastings, Physical review letters **115**, 115001 (2015).

[12] S. P. Hau-Riege, Physical Review E **87**, 4, 053102 (2013).

[13] S. Boutet, L. Lomb, G. J. Williams, T. R. Barends, A. Aquila, R. B. Doak, U. Weierstall, D. P. DePonte, J. Steinbrener, and R. L. Shoeman, Science **337**, 362 (2012).

[14] H. N. Chapman, P. Fromme, A. Barty, T. A. White, R. A. Kirian, A. Aquila, M. S. Hunter, J. Schulz, D. P. DePonte, and U. Weierstall, Nature **470**, 73 (2011).

[15] C. Caleman, N. Timneanu, A. V. Martin, H. O. Jonsson, A. Aquila, A. Barty, H. A. Scott, T. A. White, and H. N. Chapman, Optics Express **23**, 1213 (2015).

[16] D. Rackstraw, O. Ciricosta, S. Vinko, B. Barbrel, T. Burian, J. Chalupský, B. Cho, H.-K. Chung, G. Dakovski, and K. Engelhorn, Physical review letters **114**, 015003 (2015).

[17] O. Ciricosta, S. Vinko, B. Barbrel, D. Rackstraw, T. Preston, T. Burian, J. Chalupský, B. Cho, H.-K. Chung, and G. Dakovski, Nature communications **7**, 11713 (2016).

[18] V. V. Karasiev, T. Sjostrom, and S. B. Trickey, Physical Review B **86**, 115101 (2012).

[19] V. V. Karasiev, T. Sjostrom, and S. B. Trickey, Physical Review E **86**, 056704 (2012).

[20] R. A. Valenza and G. T. Seidler, Physical Review B **93**, 115135 (2016).

[21] T. Bredow and A. R. Gerson, Physical Review B **61**, 5194 (2000).

[22] W. S. Fann, R. Storz, H. W. K. Tom, and J. Bokor, Physical Review B **46**, 13592 (1992).

[23] J. Faure, J. Mauchain, E. Papalazarou, M. Marsi, D. Boschetto, I. Timrov, N. Vast, Y. Ohtsubo, B. Arnaud, and L. Perfetti, Physical Review B **88**, 075120 (2013).

[24] M. Lisowski, P. A. Loukakos, U. Bovensiepen, J. Stähler, C. Gahl, and M. Wolf, Applied Physics A **78**, 165 (2004).

[25] I. Timrov, T. Kampfrath, J. Faure, N. Vast, C. R. Ast, C. Frischkorn, M. Wolf, P. Gava, and L. Perfetti, Physical Review B **85**, 155139 (2012).

[26] C. Lee, N. N. Cheng, R. A. Davidson, and T. Guo, The Journal of Physical Chemistry C **116**, 11292 (2012).

[27] M. K. K. Leung, J. C. L. Chow, B. D. Chithrani, M. J. G. Lee, B. Oms, and D. A. Jaffray, Medical Physics **38**, 624 (2011).
[28] E. A. Stern, Y. Yacoby, G. T. Seidler, K. P. Nagle, M. P. Prange, A. P. Sorini, J. J. Rehr, and A. Joachimiak, Acta Crystallographica Section D-Biological Crystallography **65**, 366 (2009).
[29] Y. Z. Finfrock, E. A. Stern, R. W. Alkire, J. J. Kas, K. Evans-Lutterodt, A. Stein, N. Duke, K. Lazarski, and A. Joachimiak, Acta Crystallographica Section D-Biological Crystallography **69**, 1463 (2013).
[30] Y. Z. Finfrock, E. A. Stern, Y. Yacoby, R. W. Alkire, K. Evans-Lutterodt, A. Stein, A. F. Isakovic, J. J. Kas, and A. Joachimiak, Acta Crystallographica Section D-Biological Crystallography **66**, 1287 (2010).
[31] C. Nave and M. A. Hill, Journal of Synchrotron Radiation **12**, 299 (2005).
[32] R. Sanishvili, D. W. Yoder, S. B. Pothineni, G. Rosenbaum, S. L. Xu, S. Vogt, S. Stepanova, O. A. Makarov, S. Corcoran, R. Benn, V. Nagarajan, J. L. Smith, and R. F. Fischetti, Proceedings of the National Academy of Sciences of the United States of America **108**, 6127 (2011).
[33] Y. Ping, A. Fernandez-Panella, H. Sio, A. Correa, R. Shepherd, O. Landen, R. London, P. Sterne, H. Whitley, and D. Fratanduono, Physics of Plasmas **22**, 092701 (2015).
[34] F. Salvat, J. M. Fernández-Varea, and J. Sempau, in *Nuclear Energy Agency Workshop Proceedings* (OECD Publishing, Paris, 2006).
[35] A. A. Lutman, R. Coffee, Y. Ding, Z. Huang, J. Krzywinski, T. Maxwell, M. Messerschmidt, and H. D. Nuhn, Physical Review Letters **110**, 134801, 134801 (2013).
[36] A. Marinelli, A. A. Lutman, J. Wu, Y. Ding, J. Krzywinski, H. D. Nuhn, Y. Feng, R. N. Coffee, and C. Pellegrini, Physical Review Letters **111**, 134801 (2013).
[37] I. Inoue, Y. Inubushi, T. Sato, K. Tono, T. Katayama, T. Kameshima, K. Ogawa, T. Togashi, S. Owada, and Y. Amemiya, Proceedings of the National Academy of Sciences **113**, 1492 (2016).
[38] P. J. Ho, E. Kanter, and L. Young, Physical Review A **92**, 063430 (2015).
[39] E. Allaria, F. Bencivenga, R. Borghes, F. Capotondi, D. Castronovo, P. Charalambous, P. Cinquegrana, M. Danailov, G. De Ninno, and A. Demidovich, Nature Communications **4**, 2476 (2013).
[40] S. Agostinelli, J. Allison, K. Amako, J. Apostolakis, H. Araujo, P. Arce, M. Asai, D. Axen, S. Banerjee, G. Barrand *et al.*, Nuclear Instruments and Methods in Physics Research Section A: Accelerators, Spectrometers, Detectors and Associated Equipment **506**, 250 (2003).
[41] F. Gao, Y. Xie, Z. G. Wang, S. Kerisit, D. X. Wu, L. W. Campbell, R. M. Van Ginhoven, and M. Prange, Journal of Applied Physics **114**, 173512 (2013).
[42] M. Prange, D. Wu, Y. Xie, L. W. Campbell, F. Gao, and S. Kerisit, in *SPIE Optical Engineering+ Applications* (SPIE, 2014), p. 92130L.
[43] R. F. Egerton, *Electron energy-loss spectroscopy in the electron microscope* (Springer Science & Business Media, 2011).
[44] J. M. Fernández-Varea, R. Mayol, D. Liljequist, and F. Salvat, Journal of Physics: Condensed Matter **5**, 3593 (1993).
[45] D. Liljequist, Journal of Physics D: Applied Physics **16**, 1567 (1983).
[46] G. D. Zeiss, W. J. Meath, J. C. F. MacDonald, and D. J. Dawson, Radiation Research **70**, 284 (1977).
[47] M. J. Berger, ESTAR, PSTAR, and ASTAR: Computer programs for calculating stopping-power and range tables for electrons, protons, and helium ions, 1992.
[48] C. H. Bak, K. Kim, K. Jung, J.-B. Kim, and J.-H. Jang, Journal of Materials Chemistry A **2**, 17249 (2014).
[49] M. Bagge-Hansen, A. Wichmann, A. Wittstock, J. R. I. Lee, J. Ye, T. M. Willey, J. D. Kuntz, T. van Buuren, J. Biener, M. Bäumer, and M. M. Biener, The Journal of Physical Chemistry C **118**, 4078 (2014).
[50] E. Prince and A. J. C. Wilson, *International tables for crystallography Vol. C* Dordrecht, Holland, (1999).

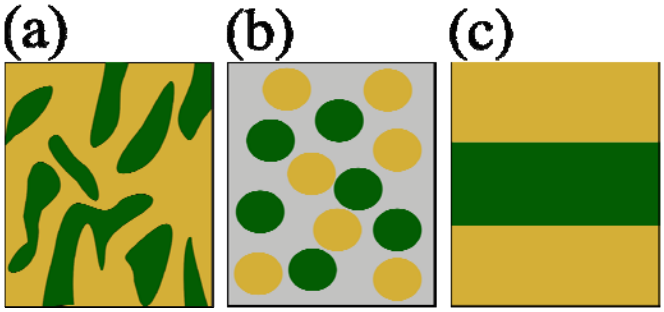

Fig. 1. Representations of three types of multicomponent targets composed of sample material (green) and heater cladding (yellow). (a): A porous subtrate filled with sample material; (b): a mixture of cladding and sample nanoparticles embedded in a solid matrix; (c): a multilayer film.

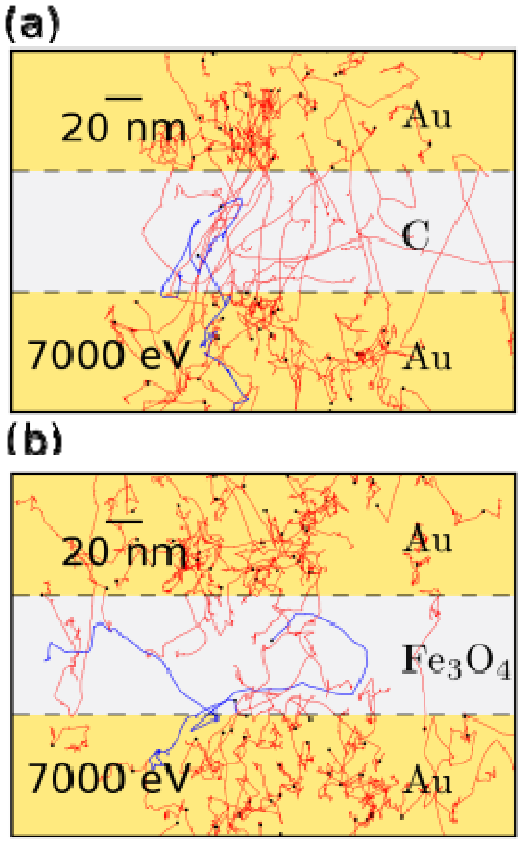

Fig. 2. Visualization of a 3-D Monte Carlo simulations of electron transport in (a) Au-diamond-Au and (b) Au-Fe-Au targets heated by 7 keV photons, incident normally from the top of the page. For readability, only 10% of tracks originating in the Au layer are displayed in (a). Electron tracks are projected onto the plane of the page; showers resulting from photoexcitation of Au and C or Fe atoms are red (thin) and blue (bold), respectively. Most electron tracks in the interior layers are due to absorption events in the Au.

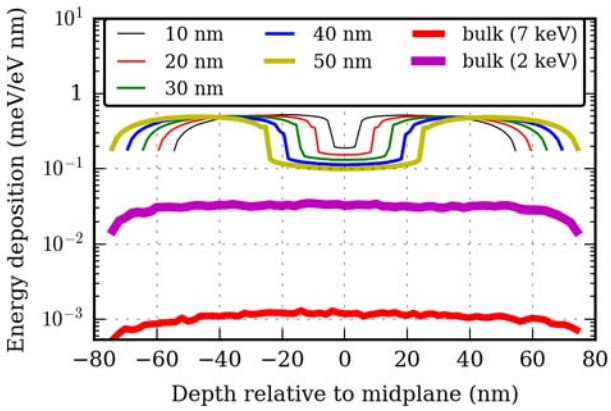

Fig. 3. Linear energy deposition due to 7 keV photons incident on an Au-C-Au target displayed for several thicknesses of the central C layer and a fixed outer cladding thickness of 50nm, compared to the linear energy deposition created by 7 keV and 2 keV photons incident on bulk C. The large, expected decrease in direct absorption of the higher-energy x-rays by the unclad samples is more than compensated by the nonlocal heating from electron transport between the Au and the interior material for the Au-C-Au target.

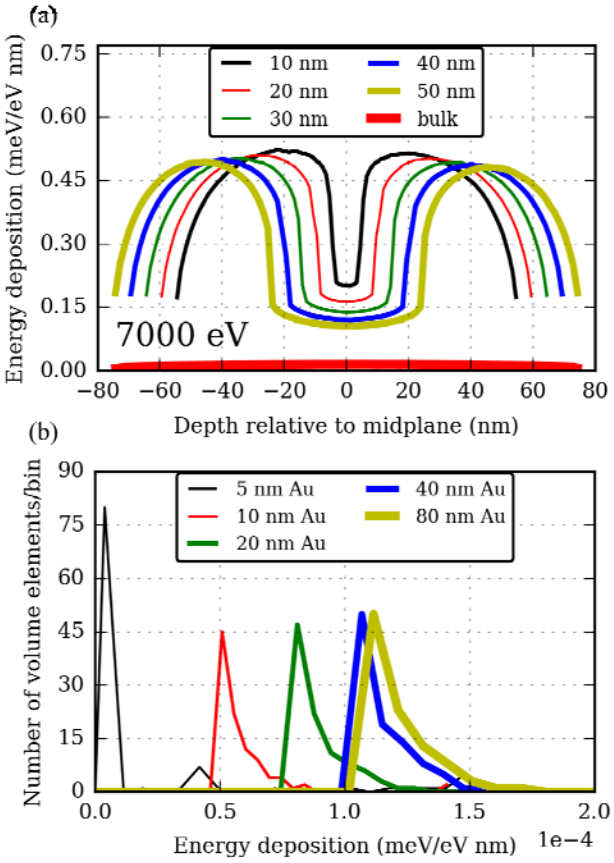

Fig. 4. (a) Linear energy deposition density generated by 7 keV photons incident on an Au-Fe_3O_4-Au target, displayed for several thicknesses of the central Fe_3O_4 layer and a fixed Au cladding thickness of 50nm. (b) Histograms of energy deposition density in volume elements of the Fe_3O_4 inclusions in Au-Fe_3O_4-Au targets, displayed for several thicknesses of the Au cladding and a fixed Fe_3O_4 layer thickness of 50 nm.

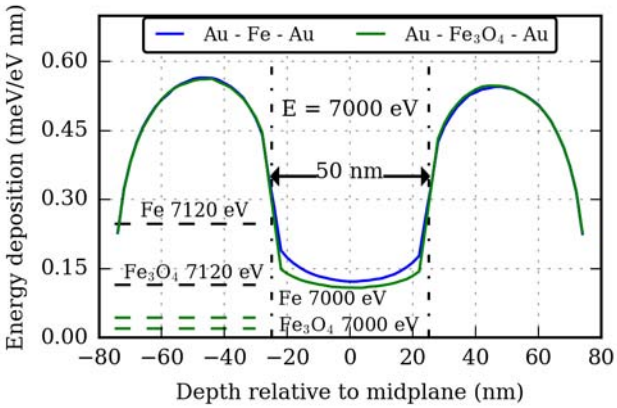

Fig. 5. Linear energy deposition in layered Au-Fe-Au and Au-Fe_3O_4-Au targets of 150 nm total thickness stimulated by 7 keV photons (solid curves). Dashed lines on the left indicate energy deposition in bulk Fe_3O_4 and Fe at photon energies of 7.12 keV (above the Fe K-edge) and 7 keV (below the edge). The multilayer configuration sufficiently enhances energy deposition so as to partially compensate for the difference between pre- and above-edge x-ray photoelectric cross sections. The benefit is particularly pronounced in Fe_3O_4 due to its much lower density and photoelectric cross-section.

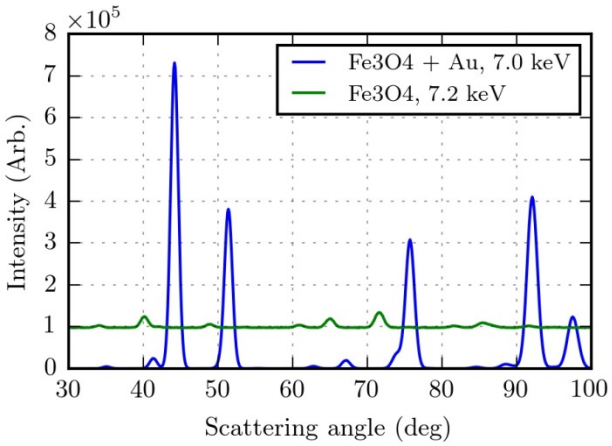

Fig. 6. Simulated powder diffraction of 50 nm Au-50 nm Fe_3O_4-50 nm Au stimulated by x-rays below the Fe K-edge (blue) compared to that resulting from photons above the edge incident on bare Fe_3O_4, including fluorescence background(green). The diffraction signal is based on empirical models for the elastic scattering form factors of Au, Fe, and O, while the fluorescence background is calculated from the tabulated *K*-shell photoelectric cross section of Fe. [50] The detector may be substantially shielded from the Au M-shell emission, and its contribution to the background is therefore neglected.